Journal of Materials Science: Materials in Electronics
https://doi.org/10.1007/s10854-018-0371-8

Low-temperature-dependent growth of titanium dioxide nanorod arrays in an improved aqueous chemical growth method for photoelectrochemical ultraviolet sensing

M. M. Yusoff[1,3] · M. H. Mamat[1,2] · A. S. Ismail[1] · M. F. Malek[1,2] · A. S. Zoolfakar[1] · A. B. Suriani[4] · M. K. Ahmad[5] · N. Nayan[5] · I. B. Shameem Banu[6] · M. Rusop[1,2]

Received: 29 June 2018 / Accepted: 13 November 2018

Abstract
The growth of titanium dioxide nanorod arrays (TNAs) in aqueous solutions containing titanium butoxide and hydrochloric acid can be controlled by regulating the temperature from 115 to 150 °C as an adjustable physical parameter. The transparent colloidal solution of titanates is clouded on the basic growth of TNAs when heated at a certain temperature using an improved aqueous chemical growth method in a clamped Schott bottle. The structural, optical and electrical properties of grown TNAs films were thoroughly investigated and discussed. The distinct and high-intensity peaks observed in the X-ray diffraction pattern and Raman spectra of the grown TNAs show the rutile phase with high crystal quality. The crystallite size, diameter size, and thickness of TNAs decrease with decreasing growth temperature. The prepared TNAs were used to detect 365 nm ultraviolet (UV) photon energy (750 μW/cm^2) in a photoelectrochemical cell structure with a maximum photocurrent of 26.31 μA and minimum photocurrent of 3.48 μA recorded for TNAs grown at 150 °C and 115 °C, respectively. The size, structural properties, charge transfer resistance, and electron lifetime play a key role in determining the UV sensing characteristics of the TNAs. Results show that TNAs are very promising in fabricating a UV sensor with a high response at 0 V bias even at a low growth temperature of 115 °C.

1 Introduction

Titanium dioxide (TiO_2) is an expedient semiconducting material for extensive applications due to the ease with which it can be utilized to form nanostructures as well as its outstanding electrical properties, such as a wide band-gap and large excitation binding energy [1–3]. The TiO_2 nanostructure possesses a high surface-to-volume ratio to form active sites for inducing the sensing mechanism. The ratio also inflicts nanoconfinement effects on the liquid molecules, which may uphold or overturn the surface reactions [4, 5]. In recent years, the aspect of nanoconfinement on photoelectrochemical cell (PEC) reactions in nanorod structures have been studied in terms of photocurrent transportation and electrolyte molecules [6–11]. A previous study has also suggested that the characteristics of nanoconfined electrolyte molecules diverge significantly than in their bulk counterpart as a result of interfacial reactions at the surface of TiO_2 nanorod structure [12–16]. Although the nanoporous structure offers a high surface-to-volume ratio, the transportation mechanism of charge carriers is not in favour due to the formation of multiple paths and electron traps between

✉ M. H. Mamat
mhmamat@salam.uitm.edu.my

1 NANO-ElecTronic Centre (NET), Faculty of Electrical Engineering, Universiti Teknologi MARA (UiTM), 40450 Shah Alam, Selangor, Malaysia

2 NANO-SciTech Centre (NST), Institute of Science (IOS), Universiti Teknologi MARA (UiTM), 40450 Shah Alam, Selangor, Malaysia

3 Kulliyyah of Engineering, International Islamic University Malaysia (IIUM), 50728 Kuala Lumpur, Malaysia

4 Nanotechnology Research Centre, Faculty of Science and Mathematics, Universiti Pendidikan Sultan Idris (UPSI), 35900 Tanjung Malim, Perak, Malaysia

5 Microelectronic and Nanotechnology – Shamsuddin Research Centre (MiNT-SRC), Faculty of Electrical and Electronic Engineering, Universiti Tun Hussein Onn Malaysia (UTHM), 86400 Batu Pahat, Johor, Malaysia

6 Department of Physics, B.S. Abdur Rahman Crescent Institute of Science & Technology, Vandalur, Chennai 600 048, India

Published online: 17 November 2018

the grain boundaries [17, 18]. Thus, the characteristics of TiO_2 nanorod arrays (TNAs), which offers direct pathways for the transportation of charge carriers, and electrolyte molecules at the vicinity of their interface play a significant role in the performance of TNAs-based applications. The utilization of TNAs is considered as an effective route for reducing the electron–hole recombination, particularly for PEC-based devices.

Recently, TNAs has been attracting a lot of interest for the application of PEC-based self-powered ultraviolet (UV) sensor devices, which don't need additional power sources or batteries, making this type of material as part of the device applicable for large-scale applications. For example, Chen et al. fabricated self-powered PEC-type UV sensor using rutile TNAs grown on SnO nanotube [19]. The fabricated device shows promising results for 365-nm UV detection with a maximum responsivity value of 0.145 A/W. In other report, Chen et al. fabricated self-powered PEC-type UV sensors using rutile TNAs [20]. The TNAs-based devices were well-responsive to the 340-nm UV light and the response of the devices was further enhanced by using SnO_2–TiO_2 heterojunction. The PEC-based sensors utilizing TNAs also developed by Wang et al. [21]. The TNAs-based devices showed good current responses to the UV light. The TNAs were hydrogenated and coated with gold nanoparticles to improve the sensing performance. The PEC-based devices, which used TNAs as a main material, have also been used in other applications such as solar cells [6, 7], hydrogen generators [8, 9], biosensors [10], and glucose sensors [11]. The TNAs of the UV sensor device produces photocurrent from the photon energy of UV. The value of photocurrent is highly dependent on the specific diameter size and length of the TNAs. Although extensive investigations have reported improvements to the single-step growth method of TNAs [12–15], the introduced method often includes a difficult preparation process and complicated equipment to enhance the deposition process on the substrate. In most cases, the application of a high-pressure vessel or autoclave was commonly reported. The operation of the tools is difficult due to the size and weight of the stainless-steel materials. Furthermore, the system also requires a Teflon vessel to hold the heat and the pressure inside the stainless-steel container. In addition, the time it takes to heat the autoclave during the growth process and to cool down the autoclave after the growth procedure prolongs and thus affects the growth of TNAs. In order to further simplify the growth of TNAs, it is essential to improve the current method to be less complicated and more rapid for the growth of TNAs on the substrate. Moreover, the expedient procedure of large-scale growth of TNAs still remains a challenge.

Several attempts have been made to further enhance the photocurrent of TNA-based UV sensors. Xie et al. reported a UV sensor based on TiO_2 nano-branched arrays on TNAs to increase the effective surface area [12]. Meanwhile Yan et al. fabricated a self-powered UV sensor based on reduced TiO_2 nanorods to improve the separation and recombination of excitonic charge carriers [22]. Although the responsivity is improved via these techniques, the preparation procedure often requires additional and advanced processes. The controllable growth of TNAs by the hydrothermal method at various parameters was also reported by Cao et al. [15]. Although the optimization of growth parameters was systemically studied, a limited number of samples were involved in the investigation. Moreover, detailed studies on the structural and electrical properties of TNAs on transparent conducting substrates using the aqueous chemical-based immersion method are rarely reported. In addition, more research should be performed to optimize the size and length of the nanorods for a specific application of the device.

In this study, we have investigated the effect of growth temperature on the properties of grown TNAs through an improved one-step aqueous chemical immersion method using a simple modified Schott bottle with cap clamps. The TNAs were deposited directly on a fluorine-doped tin oxide (FTO) substrate without a seed layer, which is a prerequisite for fabricating electronic devices, particularly for UV photosensing whereby the FTO acts as an electrode with an Ohmic contact. Particularly in this study, we investigate the influence of a low growth temperature (below 150 °C) on the structural, optical, and electrical properties of the synthesized TNAs; this task must be done in advance for the specific application of the UV photosensor. The low growth temperature could be achieved through our introduced method. The transformation process from low density to high density in correlation with decreasing growth temperature due to the reduced diameter size of TNAs has previously not been discussed in significant detail. Although the decrease of diameter size and length of the TNAs is expected to reduce the photogenerated current in attribution to the decrease of active surface area, the minimum parameter of the growth temperature, and its effect on the PEC-based UV photosensing need to be investigated for the future application of sensing devices, when low photocurrent signal is sufficient to achieve meaningful detection within modern-generation micro-controllers. Additionally, a low temperature is preferable to most of the manufacturing industries to minimise the operation costs. To the best of our knowledge, the low-temperature growth of TNAs has not been thoroughly investigated yet, and the minimum diameter size and length, or thickness of the TNAs achieved through our introduced method is by far the lowest value attained on a seedless FTO-coated glass substrate.

2 Experimental details

2.1 Synthesis of TNAs

Firstly, the TNAs were grown on a cleaned FTO-coated glass substrate using the one-step aqueous chemical growth method in a clamped Schott bottle. Briefly, a diluted hydrochloric acid (HCl; 37%, Merck) solution was prepared by adding deionized water (DI) at a volume ratio of 1:1 and was stirred for 10 min at ambient temperature in the Schott bottle. Then, 0.07 M of titanium (IV) butoxide (97%, Sigma-Aldrich) was slowly added to the diluted solution and stirred for another 30 min. An ultrasonically cleansed FTO glass substrate was immersed and placed in the prepared solution with the conductive side facing upward. The bottle was tightly closed and clamped before being heated for 3 h in an electric oven. The growth temperatures were 115 °C, 120 °C, 130 °C, 140 °C, and 150 °C. After the heating process, the bottle was cooled down to ambient temperature. The grown TNAs samples were taken out immediately, rinsed with DI water and dried at room temperature before being annealed in a furnace at 450 °C for 1 h to improve the crystallinity.

2.2 Device fabrication

The setup of grown TNAs for sensing UV irradiation was assembled based on the PEC structure. Briefly, the grown TNAs on the FTO glass substrate were exploited as a working electrode, and a platinum (Pt)-coated FTO substrate was utilized as a counter electrode. The counter electrode was produced by depositing a 100 nm thick Pt layer on the FTO glass substrate using a thermal evaporator (ULVAC). A spacer (Surlyn, DuPont) was sandwiched between the prepared electrode and counter electrode to inhibit internal short circuits. Finally, a liquid electrolyte solution comprising iodine (0.05 M), lithium iodide (0.5 M) and acetonitrile was injected into the inter-electrode spacer. The effective area of the UV sensor was designed to be approximately 1.0 cm^2.

2.3 Characterization

The structural properties were examined by field-emission scanning electron microscopy (FESEM, JEOL JSM-7600F) for surface morphology, field-emission transmission electron microscopy (FETEM, JEOL JEM-2100F) with selected area electron diffraction (SAED) for atomic structure, and X-ray diffraction (XRD, Shimadzu XRD-6000, Cu Kα radiation, wavelength 1.54 Å) for crystal structure. The structural fingerprint was also examined via and micro-Raman spectroscopy (Renishaw, 514 nm laser). The optical properties were measured using a UV-Vis-NIR spectrophotometer (Cary 5000). The electrical properties were measured using a direct current (DC) two-probing system semiconductor device analyzer (Keysight B1500A) for current–voltage (I–V) characteristics of the grown TNAs samples and UV photocurrent measurement system (Keithley 2400) under UV lamp (365 nm, 750 μW cm^{-2}) for measuring the photocurrent of the set-up PEC device samples. The surface reaction of TNAs with the electrolyte was also measured using electrochemical impedance spectroscopy (EIS) analysis (Solatron-Si1287/Si1260) under the UV lamp.

3 Results and discussion

Figure 1a–e depict the FESEM surface morphology images of grown TNAs at various growth temperatures of 115 °C, 120 °C, 130 °C, 140 °C and 150 °C samples, respectively. The grown TNAs have tetragonal-shaped structure and are uniformly grown on the FTO-coated glass substrate. The TNAs deposited at growth temperatures of 115 °C, 120 °C, 130 °C, 140 °C and 150 °C have average diameters of nearly 33 nm, 75 nm, 107 nm, 113 nm and 160 nm, respectively. These results designate that the size of the nanorods linearly increases with increasing growth temperature. All grown samples display the formation of TNAs with a comparatively high surface area and porosity, which act as efficient light-trapping structures, in addition to their excellent electron transportation behaviour. Figure 1f depicts FETEM image of the as-prepared TNAs grown at 150 °C, which clearly shows the well-defined TiO_2 nanorod. The SAED pattern of the TNAs (insert Fig. 1f) provides a clear diffraction spot corresponding to rutile TiO_2, which demonstrates that the nanorods are rutile TiO_2 with (001)-oriented crystal.

Figure 2a–e display the cross-sectional images of grown TNAs at various growth temperatures of 115 °C, 120 °C, 130 °C, 140 °C, and 150 °C samples, respectively. The growth temperature plays a significant role in increasing the length of TNAs. The average length of TNAs showed increased rapidly with increasing growth temperature with average lengths of 0.27 μm, 0.41 μm, 0.79 μm, 1.93 μm and 2.11 μm at growth temperatures of 115 °C, 120 °C, 130 °C, 140 °C, and 150 °C samples, respectively (Table 1). The higher energy provided in higher growth temperatures enhanced the kinetic energy of the system and accelerated the growth reaction process, which increases the mobility and the diffusion length of the precursor ions to reach the firstly grown TNAs nuclei. The cross-sectional images also demonstrate that the aligned TNAs are vertically grown on the FTO glass substrates, which are likely to improve the electron transportation that could be attributed to a single pathway of nanorod structure [23]. The cross-sectional images are also consistent with the top-view morphological

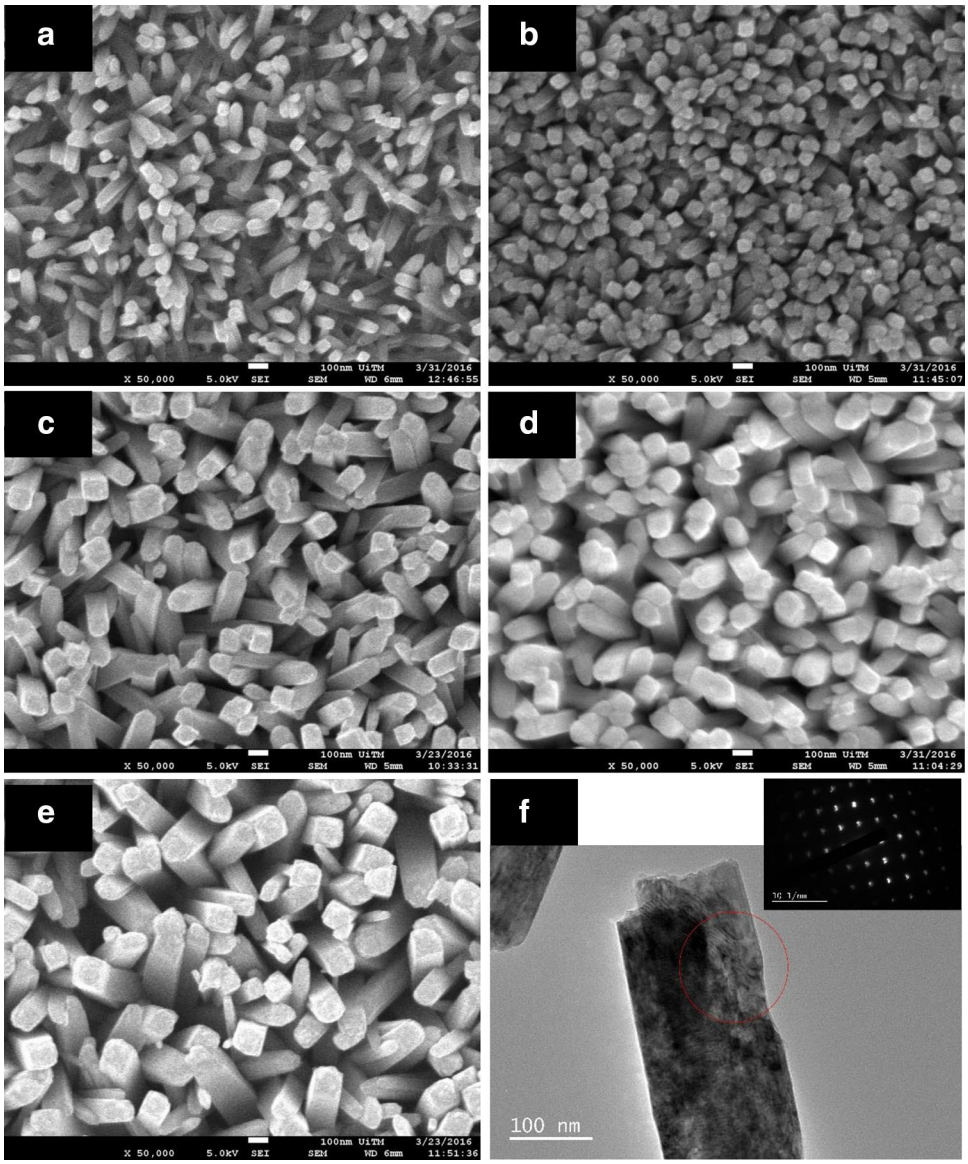

Fig. 1 Surface morphology of TNAs at growth temperature of **a** 115 °C, **b** 120 °C, **c** 130 °C, **d** 140 °C and **e** 150 °C. **f** FETEM image of as-prepared TNAs (Inset image: SAED pattern of the TNAs)

images, which exhibit the increasing growth of TNAs size in correlation with the growth temperature. The correlation between average diameter and length of TNAs with the growth temperature are depicted in Fig. 2f. The minimum growth temperature that can be applied to grow TNAs for the current study using the introduced method was 115 °C. However, our experiment suggested that the formation of TNAs has not been observed on the substrate at growth temperatures below 115 °C (the result is not provided here). In this view, our results suggest that there is a critical growth temperature, which provides adequate thermal energy for TNAs formation by facilitating efficient adsorption of precursor ions for surface stabilization. At a temperature below 115 °C, there is insufficient thermal energy to effectively support the adsorption of precursor ions on the substrate to form TNAs.

Figure 3 presents the XRD pattern of the grown TNAs at various growth temperatures. Four diffraction peaks were recorded in the pattern, which correspond to (110), (101), (211), and (002) planes. These planes are matched to the tetragonal-faceted nanorods of rutile TiO_2 (JCPDS No. 01-072-1148). The peaks indicating the presence of anatase and brookite structures were not observed in the XRD pattern. Meanwhile, the peaks marked with stars designate the SnO_2 peaks arising from the FTO glass substrate. Based on the XRD peaks, the edge-sharing formation of the octahedron had manifested in the growth reaction process of rutile TNAs. TiO_6 octahedrons in rutile framework bond to each other through edge-sharing, which result in the formation of chains along the *c*-axis. The vertically grown TNAs along the *c*-axis is represented by the (002) peak, and the intensity of the peak has been reported to correspond with

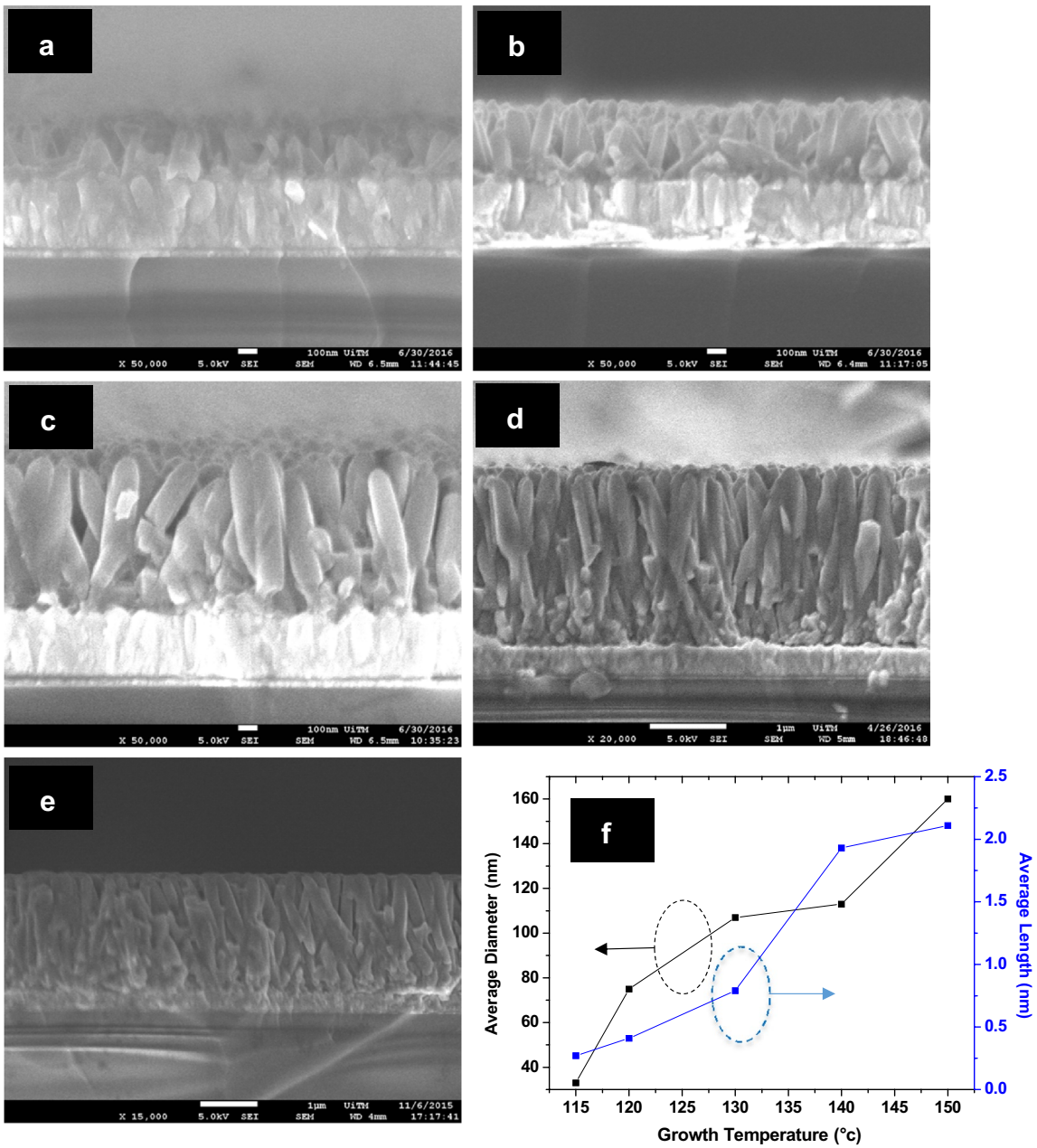

Fig. 2 Cross-section images of TNAs at growth temperature of **a** 115 °C, **b** 120 °C, **c** 130 °C, **d** 140 °C and **e** 150 °C. **f** Average diameter and length at various growth temperatures

Table 1 Average diameter, average length and optical bandgap of TNAs at various growth temperatures

Growth temperature (°C)	TNAs average diameter (nm)	TNAs average length (μm)	Optical bandgap energy (eV)
115	33	0.27	3.42
120	75	0.41	3.38
130	107	0.79	3.02
140	113	1.93	3.05
150	160	2.11	3.00

the number of grown TNAs in proportion to the growth temperature [24, 25]. The (002) diffraction peak of the TNAs appears to intensify as the growth temperature increases, which proves that the grown TNAs are well-orientated along the *c*-axis at high temperature. The TNAs are also represented by the (101) peak, which resulted from the X-rays penetrating into the side surface of the TNAs [24, 26]. The samples also exhibit distinct peaks at (110), and (211), indicating the growth of TNAs on other planes as discussed in previous reports [15, 27, 28]. The availability

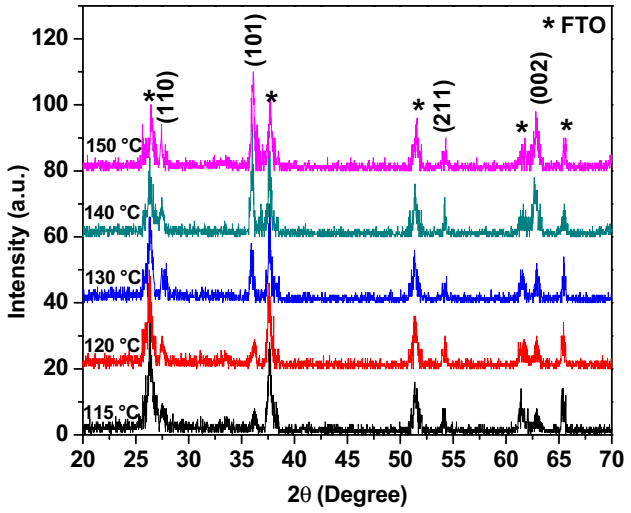

Fig. 3 XRD patterns of TNAs samples

of corners and edges from the octahedral structure influence the growth rate of TNAs through the merging activity of the unit cell of the TiO_6 octahedron via edge-sharing and could be increased at a high growth temperature. Thus, the growth of rutile TNAs corresponding to the XRD peaks is likely to follow the sequence of (110) < (100) < (101) < (001) [29]. This sequence corresponds to the rutile TNAs, which are represented by the [101] and [001] directions that were uniformly grown on the surface of the substrate, even at the lowest growth temperature. In addition, the TNAs have the tendency to grow on the FTO glass substrate at various growth temperatures as specified because of a small lattice mismatch between FTO and TNAs at 2% [30]. The FTO layer also helps to improve the crystallinity of rutile-type TNAs on the glass substrate. A previous study indicates that the atomic arrangement of the TiO_2 is strongly influenced by the crystallinity of the substrate [31]. The FTO has an almost similar tetragonal structure with rutile TiO_2 with lattice parameters of $a = b = 0.4687$ nm, which slightly differ from the lattice parameters of rutile TiO_2 ($a = b = 0.4594$ nm). Thus, the growth of TNAs on the FTO glass substrate is possibly due to this small lattice mismatch to the extent of the minimum growth temperature. The FTO thus facilitates a nucleation layer to grow rutile TNAs effectively without the need of a TiO_2 seed layer.

When the reagents titanium (IV) butoxide, HCl, and DI water are mixed, the following reactions take place [32, 33]. The $4s^2$ and $3d^2$ orbitals of titanium from the precursor (titanium (IV) butoxide) undergo an octahedral d^2sp^3 hybridization. The four valence electrons at equatorial hybrid orbitals are shared by $OC_4H_9^-$ ligands, which have high electronegativity [34]. Meanwhile, the two axial orbitals in this configuration are still empty. When the DI water is added, spontaneous hydrolysis occurs to the Ti^{4+} ions. The $OC_4H_9^-$ ligands in the precursor that attached to the Ti^{4+} ions are replaced by OH^-, which readily dissociate from H_2O and has strong nucleophilic properties. The $OC_4H_9^-$ ligands react with H^+ generated from H_2O dissociation to form C_4H_9OH. The Ti^{4+} ions have six bonding orbitals available, which consists of four equatorial orbitals and two axial orbitals. These Ti^{4+} ions are inclined to form octahedral complexes with ligands. With the four valence electrons at equatorial hybrid orbitals bonded to strongly nucleophilic OH^- ligands, the two axial orbitals remain available and tend to bond with weak nucleophilic ligands such as OH_2 (aquo) in the aqueous solutions. As a result, a hydroxo-aquo $[Ti(OH)_4(OH_2)_2]^0$ complex with neutral charge is formed through this process. The TiO_2 can be formed from the condensation process of a hydroxo-aquo $[Ti(OH)_4(OH_2)_2]^0$ complex under a supersaturation condition.

However, the condensation process will rapidly occur if the solution has low acidity and consequently produce amorphous TiO_2 particles [35]. According to Liu et al., the TiO_2 precipitated immediately upon the direct addition of titanium butoxide into DI water; this solution produced no nanorods on the substrate after the hydrothermal process [30]. With the presence of HCl, the growth of rutile phase crystalline TiO_2 on the substrates could be achieved because HCl reduces the spontaneous condensation in the solution by producing more complexes with a positive charge [36]. The high acidity of the solution also allows the formation of stable linear edge-shared configurations, which produces rutile TiO_2 because the strong repulsion forces between positively charged complexes are not stable for the angular configuration that produces anatase TiO_2. In general, the HCl functions as a crystallization inhibitor by reducing the concentration of OH^- anions in the solution and prevents rapid condensation of titanium–hydroxo complexes through the protonation of OH^- ligands to increase electrostatic repulsion between the complexes. Thus, with the help of HCl as a crystallization inhibitor, $[Ti(OH)_{4-n}(OH2)_{2+n}]^{n+}$ |n = 1, 2, 3 complexes can be produced in the solution, which carry positive charge and control the reaction by hydrolysis equilibrium [37, 38]. These $[Ti(OH)_{4-n}(OH2)_{2+n}]^{n+}$ |n = 1, 2, 3 complexes avoid each other due to electrostatic repulsion and remain stable in the solution, particularly before the immersion process. Therefore, the solution remains transparent in the presence of HCl. Other reports also suggest that in aqueous titanium (IV) butoxide solution with the presence of HCl, Cl^- anions are coordinated to the Ti^{4+} ions to form $[Ti(OH)_nCl_m]^{2-}$, where $n + m = 6$ [39]. The n and m values are influenced by the solution acidity and Cl^- ions concentration in the solution. However, another study indicates that Cl^- ions are more protonated in water rather than coordinated to the Ti^{4+} ions [37]. This condition was supported by Jordan et al., which also showed that Cl^- ions were not coordinated to the Ti^{4+} ions in the Ti-polycondensate structures [32]. The results suggested that Cl^- unlikely coordinated to the

Ti^{4+} cations. Upon the immersion process at a certain growth temperature, the energy supply through the heating process is adequate to overcome electrostatic repulsion forces between the $[Ti(OH)_{4-n}(OH2)_{2+n}]^{n+}$ |n = 1, 2, 3 complexes and facilitate the condensation process of rutile TiO_2 on the FTO substrate. These processes are accelerated at higher growth temperatures as manifested by the enlarged diameters and lengths of the TNAs. The condensation process starts with removal of OH_2 (aquo) ligands from the complexes through an olation process. As a result, the octahedral chains are formed. Then, the oxolation process takes place to remove the remaining OH (hydroxo) ligands from the complexes to produce the nanorod structure in the process through multiple combinations of titanium-octahedral chains.

The XRD data of grown TNAs at different growth temperatures has been employed for calculating the lattice parameters of *a*-axis and *c*-axis based on the distinctive peaks of (110) and (002) planes of the XRD spectra, respectively, using the following equation [40, 41]:

$$\frac{1}{d^2} = \frac{h^2 + k^2}{a^2} + \frac{l^2}{c^2} \tag{1}$$

where *d* is the distance between the planes based on 2θ from the Bragg Law in Eq. (2), while *h, k*, and *l* represent Miller indices.

$$d = \frac{\lambda}{2\sin\theta} \tag{2}$$

The estimated values of lattice parameters in Table 2 disclose that there has been a steady increase from 4.594 to 4.653 Å and 2.962 to 2.976 Å for the *a*-axis and *c*-axis of grown TNAs, respectively. These results show that a positive correlation was found between the growth temperature of TNAs, and the lattice parameter for both *a*-axis and *c*-axis. The measurement of strain (ζ_c) at the *c*-axis in rutile TNAs was chosen to determine the correlation between growth temperature and strain from the calculated lattice parameters according to the following equation [41, 42]:

$$\varepsilon_c = \frac{c - c_o}{c_o} \tag{3}$$

here *c* represents the lattice parameter of the strained TNAs estimated from the XRD data and c_o represents the standard value of the lattice parameter for unstrained bulk rutile TiO_2. A positive sign of strain designates tensile, while a negative sign designates compressive strain. The value of strain in Table 2 shows that all samples are tensile. The strain increases from 0.060 to 0.608% with increasing growth temperature from 115 to 150 °C samples (Fig. 4), indicating the formation of a more tense structure with a high growth temperature of the solution during the reaction. Thus, a more relaxed structure could be achieved at low growth temperatures. The strain values also designate that the lattice parameter, *c*, of the TNAs is elongated along the unit cell of the *c*-axis. The formation of strain also contributes to the existence of distortion in a unit cell structure due to the deviation of interplanar distance (*d*) of grown TNAs at various growth temperatures, compared to bulk TiO_2. The distortion is calculated based on the lattice mismatch (Δd) using the following equation [43]:

$$\Delta d = \frac{d - d_o}{d_o} \times 100\% \tag{4}$$

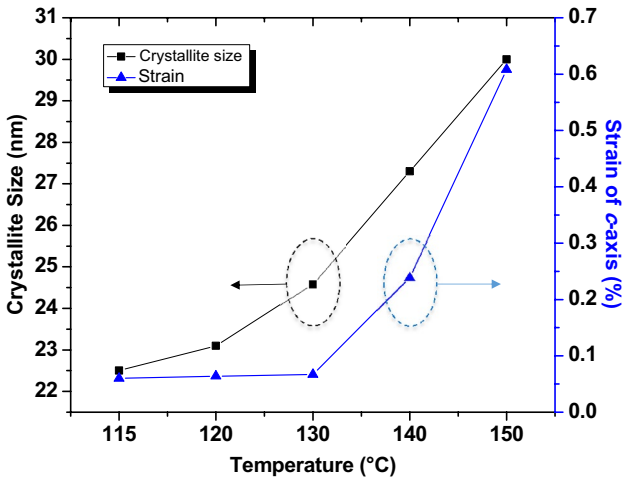

Fig. 4 Variation of the crystallite size and strain of the grown TNAs with various growth temperatures

Table 2 Relative peak intensity, crystallite size, strain, lattice mismatch, and lattice parameters of the TNAs samples

Growth temperature (°C)	Relative peak intensity, $P_{(hkl)}$	Crystallite size, D (nm)	Strain of *c*-axis, ε_c (%)	Lattice mismatch, Δd (%)	Lattice parameters		
					a (Å)	*c* (Å)	*c*/*a*
115	0.778	22.5	0.060	0.013	4.594	2.962	0.645
120	0.782	23.1	0.064	0.017	4.596	2.963	0.645
130	0.793	24.6	0.067	0.020	4.597	2.964	0.645
140	0.825	27.3	0.240	0.493	4.649	2.965	0.640
150	0.830	30.0	0.608	0.561	4.653	2.976	0.640

where d is the interplanar distance of rutile TNAs obtained from the XRD data and d_o is the interplanar distance of the standard bulk rutile TiO_2. A positive value designates that the residual stress is tensile, while a negative value designates that the residual stress is compressive on the surface of grown TNAs at various growth temperatures. The analysed data on the lattice mismatch in Table 2 indicate that the residual stress in all samples is tensile. The generation of strain and lattice mismatch due to the alteration of lattice parameter from its standard bulk value are likely to be related to the existence of microstress and macrostress from the broadening of diffraction peaks as the growth temperature increases. These stresses may partly be explained by the generation of defects in the grown TNAs and may facilitate inferences on its unit cell structure to depart from its ideal stoichiometry. Macrostress extends the average crystallite size, while microstress broadens the diffraction peak [43, 44].

Monocrystalline structure is mostly thermodynamically stable due to the benefits of low surface and interface energies compared to polycrystalline structure [42, 45]. The influence of strain energy minimisation is proportional to those of surface and interface energy minimisation since the normal growth of crystallites could not occur until the subpopulation of crystallites favoured by strain energy minimisation had been dissipated with other orientations. In the course of tolerably thin films, surface and interface energy minimisation of crystallites are meticulously developed, while the strain energy minimisation of crystallites is structured for thicker films at high elastic strain [46]. Consequently, the duel between surface and interface energy minimisation, and strain energy minimisation of the crystallites is likely to be related to the formation of strain and expansion of lattice parameters as evaluated by the analysis of XRD at various growth temperatures. This may also be connected to the rise of (110), (101) and (211) peaks in correlation with the average length of nanorods. It can thus be suggested that the probability of the TNAs growth process along the c-axis is mostly subjected to the surface and interface energy minimisation, while others are subjected to the strain energy minimisation. During the initial growth of TNAs, the agility of adatoms is low and donates to surface and interface energy minimisation on the surface of FTO glass substrate for the growth of grains. In addition, the agitation of HCl in correlation with growth temperature also streams the pressure inside the glass container and may affect the strain energy minimisation for TNAs growth due to the high agility of adatoms on a crystal surface.

The XRD patterns of grown TNAs at various growth temperatures also has been utilized to calculate the relative peak intensity, $P_{(hkl)}$, of the c-axis along the (002) plane, which has been described to substantially improve the electrical mobility [47, 48], according to the following equation [49]:

$$P_{(hkl)} = \frac{I_{(hkl)}}{\sum I_{(hkl)}} \tag{5}$$

here $I_{(hkl)}$ corresponds to the peak intensity of the (002) plane, while $\Sigma\, I_{(hkl)}$ represents the total peak intensities of all planes of the grown TNAs on the substrate. The average crystallite sizes of the grown TNAs at various growth temperatures have also been analysed using Scherrer's equation as follows:

$$D = \frac{0.94\lambda}{\beta \cos\theta} \tag{6}$$

where λ, β, and θ represents the wavelength of the X-ray (1.54 Å), full width at half maxima (FWHM) of (002) plane, and peak angle of the (002) plane. Table 2 displays the measured values of the relative peak intensity and average crystallite sizes for TNAs grown at different temperatures. The results of the relative peak intensity of grown TNAs illustrate a small increase from 0.78 to 0.83, while the average crystallite size linearly increases with growth temperature in the range of 22.5–30.0 nm for 115–150 °C samples (Fig. 4), respectively. The results of average crystallite size further describe the growth mechanism in the solution-based immersion method, which is nucleation and crystallization. Throughout these processes, the enlargement of the crystallite size at high growth temperature was hastened by the increase of nucleation number per unit area to continually form crystal nuclei [50, 51]. Additionally, the increase of average crystallite size with increasing growth temperature could be attributed to the lengthened lattice parameters of a-axis and c-axis as analysed through the XRD patterns. The divergence of lattice parameters describes the foundation of defect formations containing oxygen content in the grown samples [40]. Furthermore, the XRD combined patterns of rutile TNAs peaks for all samples show the slight shift of peaks towards the standard value of bulk TiO_2 peaks as the growth temperature decreases to the smallest value. A possible explanation for this result may be the relaxation of crystallite structure of the TNAs. This condition subsequently decreases the surface energy and the tensile stress of the grown TNAs [42], which is in agreement with our strain analysis.

Figure 5 shows the Raman spectra of grown TNAs at various growth temperatures. The rutile structure of TiO_2 is categorized under P42/mnm tetragonal space group. In this group, the unit cell is constructed by two lattice vectors of $\boldsymbol{a}$ and $\boldsymbol{c}$. Generally, the unit cell contains two TiO_2 units, where Ti ions positioned at (0, 0, 0) and (1/2, 1/2, 1/2), while O ions located at $\pm$(u, u, 0) and $\pm$(1/2 + u, 1/2 − u, 1/2), where u ≈ 0.305 nm [52]. Therefore, four Raman active modes could be observed in the frequency region of 100–700 cm^{-1}, namely B_{1g}, two-phonon bands (marked as *), E_g, and

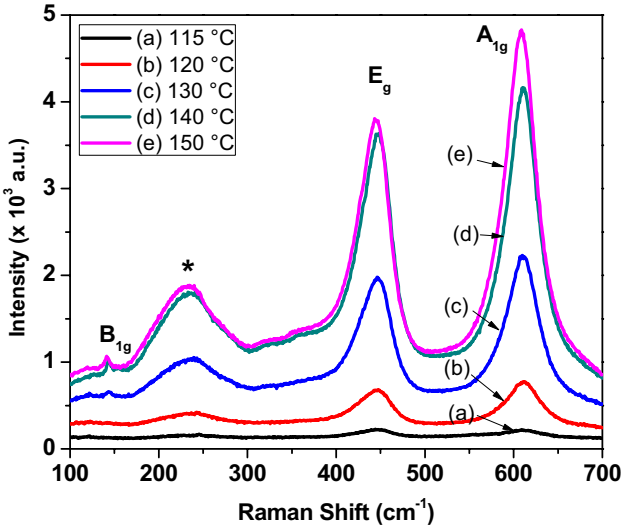

Fig. 5 Raman spectra of TNAs samples at different growth temperatures

A_{1g}. From Fig. 5, all grown TNAs samples show distinct rutile structure through the Raman peaks at approximately 143 cm^{-1} (B_{1g}), 235 cm^{-1} (two-phonon bands), 447 cm^{-1} (E_g) and 612 cm^{-1} (A_{1g}) [53, 54]. Prominent peaks can be observed for E_g and A_{1g}, which are considered as characteristic peaks of rutile TiO_2. The E_g and A_{1g} are nonpolar and polar modes, respectively; these peaks involve vibrating O ions and stationary Ti ions in the lattice. The peak of E_g represents the vibration mode of the Ti–O stretch, while A_{1g} indicates the vibration mode of released oxygen atoms from the phase along the *c*-axis. These peak positions are in good agreement with the E_g (447 cm^{-1}) and A_{1g} (612 cm^{-1}) values of bulk rutile TiO_2. The two-phonon bands in the Raman spectra however, translated into broad peaks in the spectra. Nevertheless, the peak of B_{1g} is relatively small and absent for 115 °C and 120 °C samples. This peak of B_{1g} is related to vibration mode of O–Ti–O bond bending. Other peaks indicating the structures of anatase and brookite of TiO_2 are undetectable on the spectra, which are in agreement with the XRD's result. The frequency shift of Raman bands for the grown TNAs at various growth temperatures is shown in Table 3. The frequency shifts of distinct E_g and A_{1g} peaks are red-shifted for all the grown samples as compared to the bulk counterpart. The redshift increased gradually as the growth temperature is increased. In essence, the red-shifting of the E_g and A_{1g} peaks is likely to be related to a phonon confinement effect and oxygen vacancy defects in rutile TiO_2 structures [55, 56]. Furthermore, the red-shifts may partly be explained by the tensile stress being influenced by the surface stress [57], which agrees with our XRD analysis at various growth temperatures. The broad peak position at 235 cm^{-1} for two-phonon bands also red-shifted

Table 3 Raman bands of prepared TNAs grown at different growth temperatures

Growth temperature (°C)	Raman bands of prepared rutile TNAs			
	B_{1g} (cm^{-1})	Two-phonon bands (*) (cm^{-1})	E_g (cm^{-1})	A_{1g} (cm^{-1})
115	–	234.5	446.7	611.6
120	–	234.0	446.7	611.6
130	142.9	234.0	446.1	611.6
140	142.3	233.5	445.6	610.5
150	141.7	233.5	445.6	610.5

and intensified as the growth temperature increased, which may be attributed to the expanded TNAs size. The analysed patterns therefore further support the suggested relationship between the frequency red-shift and average crystallite size [58] as calculated from the XRD patterns. The intensity of the Raman peaks signifies the concentration or number of molecules in the grown TNAs. The resultant Raman intensities in Table 3 incrementally rise with the growth temperature for the 115–150 °C samples. A possible explanation for this might be that the penetration distance of the incident beam into the grown sample, which is higher in thicker and larger TNAs, increases the inelastic scattered light to escape from the sample.

Figure 6 displays the UV–Vis transmittance spectra of grown TNAs at various growth temperatures of 115 °C, 120 °C, 130 °C, 140 °C and 150 °C in the wavelength between 300 and 500 nm. All rutile TNAs samples can be markedly detected by the absorption of the incident beam at about 410 nm by the sharp edges, which is equal to the

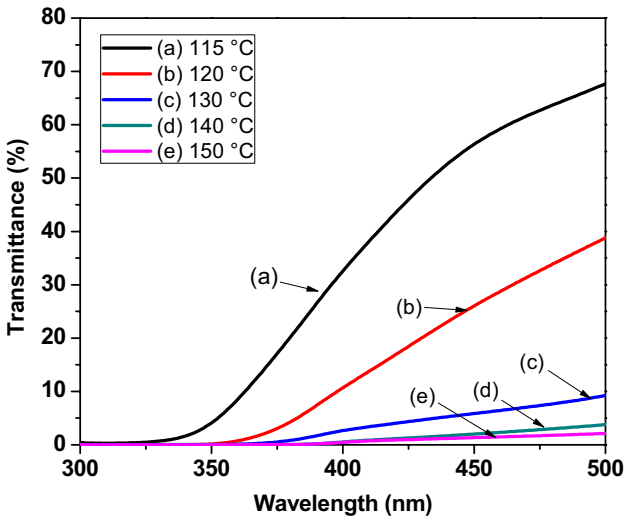

Fig. 6 UV–Vis transmittance spectra of TNAs films

3.02 eV energy gap of rutile TiO_2 [59]. The growth temperature greatly influences the fine structure in the transmittance spectra of the grown TNAs. Figure 6 exhibits a clear trend decreasing average transmittance with increasing growth temperature. The lowest transmittance can be observed in the sample grown at the maximum growth temperature in attribution to the observed elongations of the grown TNAs, as agreed with the FESEM analysis. The lengthened grown TNAs also may have increased the light scattering effect in crystallites, which reduced the transmittance of grown samples. The resultant UV–Vis spectra are used to measure the absorption coefficient using Lambert's law [60]:

$$\alpha = \frac{1}{t}\ln\left(\frac{1}{T}\right) \tag{7}$$

where t is the thickness or TNAs length and T is the transmittance of the grown TNAs sample. The absorption coefficients of grown TNAs at various growth temperatures are presented in Fig. 7. It can be seen from the result that the average absorption coefficient increases with decreasing growth temperature. The sharp slope can be seen below the UV region (<410 nm) for all grown samples. The high absorption coefficient for the grown TNAs sample at the lowest growth temperature is due to the particle size and length of the nanorod, which is the lowest of all samples; its value below 410 nm is by far the largest of all studied samples. A possible explanation for this is that the value, which is subjected to the film thickness, determines the degree of light penetration into the TNAs at a particular wavelength before being absorbed. The sharp edges are also observed to red shift toward lower wavelengths as the grown TNAs films thicken. These results are likely related to the increasing strain, as discussed in the XRD analysis previously.

The optical bandgap energy (E_g) of the grown TNAs at various growth temperatures were estimated using the Tauc plot between 300 and 500 nm using the following equation [61–63]:

$$(\alpha h\nu)^2 = A(h\nu - E_g) \tag{8}$$

where α is the absorption coefficient, $h\nu$ is the photon energy, E_g is the optical bandgap, and A is a constant. E_g was obtained from the estimated linear line of the plotted graph of $(\alpha h\nu)^2$ versus $h\nu$ for the grown TNAs samples (Fig. 8). The plotted graph displays an adequate linear line at the switching curve, inferring that the grown TNAs is in the direct bandgap in nature [64, 65]. The estimated values of the optical bandgap at various growth temperatures are presented in Table 1. The optical bandgap reduces from 3.42 to 3.00 eV with rising growth temperatures. This shrinking of the optical bandgap with respect to elevating growth temperature might be associated to the change in TNAs size, density, crystallization, oxygen vacancies, and size intensification of the scattering centre [66–68]. However, we believe that the size expansion and enhanced crystallization are the dominant mechanisms that influence the optical bandgap of TNAs. At higher growth temperatures, crystallites grow larger to improve the crystallization, which increases the size of TNAs and subsequently reduces the optical bandgap energy. The investigation of UV–Vis spectroscopy has also shown that radiation below 410 nm can be absorbed by the grown TNAs. Thus, this variation of light absorbance contributes to the generation of excitonic charge carriers based on the thickness of the grown layer.

The photoresponse properties of grown TNAs at growth temperatures of 115 °C, 120 °C, 130 °C, 140 °C and 150 °C

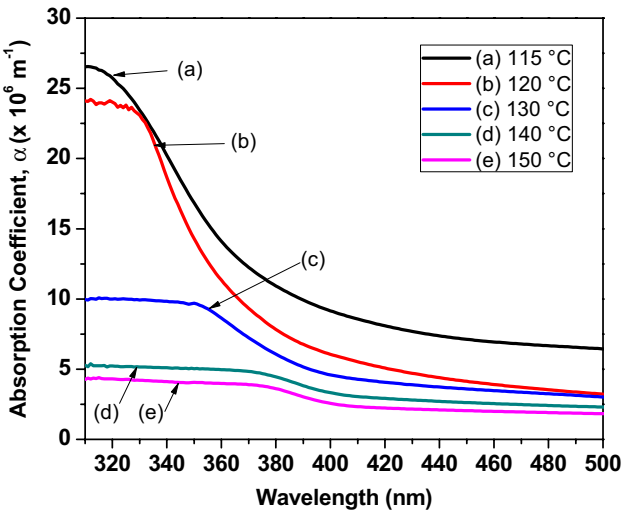

Fig. 7 Absorption coefficient α of TNAs films as a function of wavelength

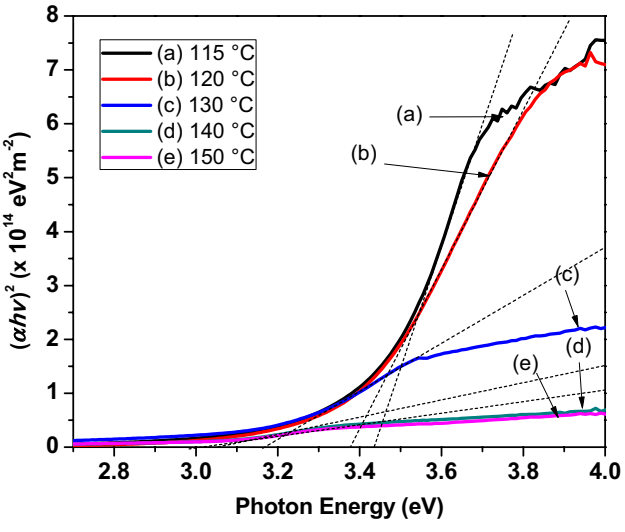

Fig. 8 Extrapolation of the optical bandgap energy E_g of TNAs films using Tauc plot

samples under the UV irradiation (365 nm, 750 μW/cm^2) was measured from the generated photocurrent under an on/off state of the UV lamp at 0 V bias in a prepared electrolyte solution containing PEC structure. From the result in Fig. 9, it is apparent that the generated photocurrent of all grown samples instantly rose and fell when switching the on/off state of the UV lamp. The photocurrent patterns are almost identical through each cycle of switching for all the samples. It can thus be suggested that the grown TNAs exhibit remarkable responses to the UV irradiation in electrolyte solutions. This generated photocurrent may be explained by the fact that UV irradiation, which exceeds the bandgap energy of the grown TNAs, is able to excite the electrons from the valence to conducting band and thereby leave holes in the valence band to form electron–hole pairs.

TiO_2 is essentially an *n*-type material and could disassociate to Ti^{3+} and oxygen vacancies (V_O) under the UV irradiation [69, 70], which could be based on the following reaction [71]:

$$Ti^{4+}O_2^{2-} \rightarrow Ti_{1-2x}^{4+}Ti_{2x}^{3+}O_{2-x}^{2-} + xV_o + 0.5xO_2 \quad (9)$$

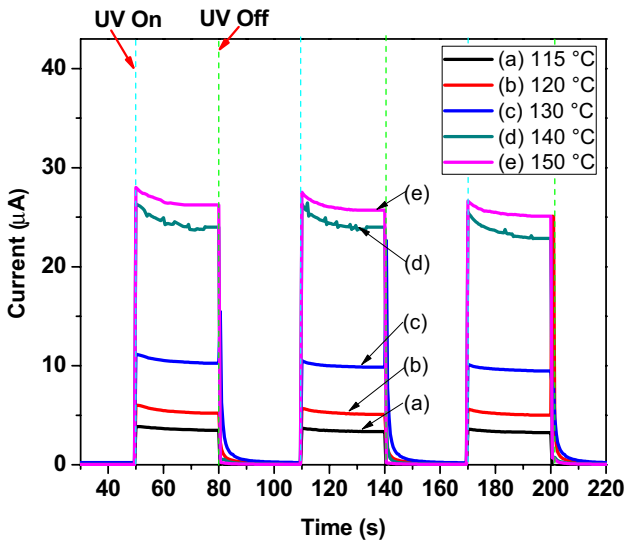

Fig. 9 Photocurrent response of the TNAs in PEC structure under UV irradiation (365 nm)

Under the exposure of UV energy, excitonic charge carriers were generated based on following equation:

$$h\nu \rightarrow e^- + h^+ \quad (10)$$

where $h\nu$ is the photon energy, e^- is the electron and h^+ is the hole. The photon energy discharges O^{2-} to produce oxygen vacancies in the grown TNAs. The photogenerated electrons move toward the FTO glass substrate through the nanorods, while the photogenerated holes diffuse toward the TNAs/electrolyte interface. The flow of photogenerated electrons through the external circuit produces the photocurrent, while the photogenerated holes diffuse into electrolytes to oxidize iodide ions in the process. The photogenerated electrons then react with the oxidized iodide ions (triodide ions) to complete the closed circuit.

Generally, the photocurrent decreases the amount of resistance upon the UV exposure and instantly returns to its initial dark current value during the "off" state [15, 72]. The values of generated photocurrent are presented in Table 4. There is a clear trend of increasing generated photocurrent from 3.48 to 26.31 μA with increasing growth temperature from 115 to 150 °C of grown TNAs samples. From this data, we can see that the grown TNAs in the 115 °C sample resulted in the lowest, while the grown TNAs at 150 °C sample resulted in the highest value of photocurrent. The increase of generated photocurrent may be explained by the expansion of the interface area in grown TNAs/electrolyte results in higher UV absorption [12]. Additionally, longer TNAs with high crystallinity can induce in a faster separation of electron–hole pairs and oriented transfer of the photogenerated charges [41]; this thus could produce a higher UV photoresponse. This outcome is in line with the enlarging sizes of grown TNAs with respect to rising growth temperature as measured with FESEM. It can thus be suggested that the surface area of grown TNAs is the main parameter in determining the generated photocurrent. The values of photocurrent show that the UV absorption of grown TNAs is improved as expected with increasing growth temperature. This result is also in agreement with the I–V measurement of grown TNAs at 115–150 °C samples, as shown in Fig. 10 at ambient temperature within the range of − 1.0 V. The plot in Fig. 10 shows a linear graph indicating the Ohmic characteristic of the grown TNAs samples. The

Table 4 Electrical properties of the grown TNAs samples

Growth temperature (°C)	Photocurrent, I_{ph} (μA)	Dark current, I_{dark} (μA)	Resistivity, ρ (MΩ cm)	Conductivity, σ (nS cm^{-1})	Responsivity, R (mA/W)	Sensitivity	Rise time (s)	Fall time (s)
115	3.48	0.015	73.15	1.37	5	232	0.15	0.91
120	5.21	0.017	80.84	1.24	7	307	0.10	0.61
130	10.26	0.024	101.72	0.98	14	428	0.05	0.31
140	24.01	0.033	164.37	0.61	32	728	0.02	0.13
150	26.31	0.036	174.26	0.57	35	731	0.02	0.12

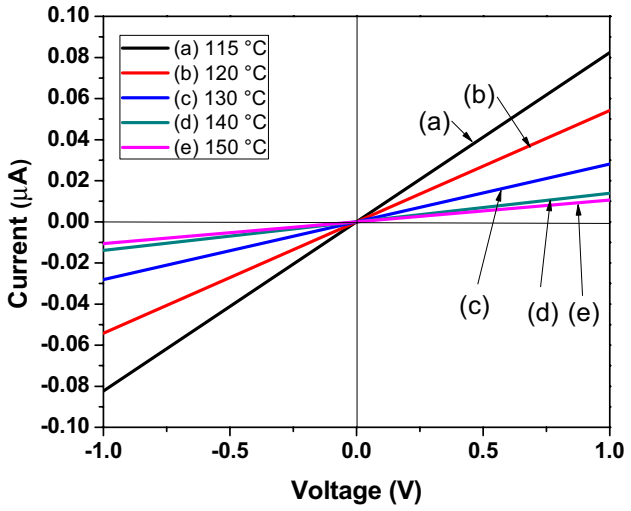

Fig. 10 I–V characteristic of TNAs

electrical properties of the samples are summarized in Table 4. From the result, it is apparent that the resistivity increases from 73.15 to 174.26 MΩ cm as the growth temperature increases from 115 to 150 °C. This result shows a positive correlation between the resistivity and growth temperature that could be attributed to the increased layer thickness of grown TNAs. The variation of resistivity may also be due to voids that ascended from periodic cylindrical nanorods on the substrate. From the photocurrent spectra, the responsivity (R) of the UV sensor was also calculated by Eq. (11) [73]:

$$R = \frac{J_{ph} - J_{dark}}{P_{op}} \tag{11}$$

where J_{ph} is the photocurrent density, J_{dark} is the dark current density, and P_{op} is the optical power density of the UV source (750 μW/cm^2). The active surface area of a TNAs-based UV sensor, which was irradiated with the UV light, is fixed at 1 cm^2. The photocurrent and dark current of 115–150 °C samples are presented in Table 4. From these values, the responsivity of the UV sensor increases from 5 to 35 mA/W as the growth temperature rises from 115 to 150 °C. This result indicates that the UV sensor composed of TNAs grown at 150 °C has the highest responsivity than the other samples.

The sensitivity of grown TNAs in electrolyte solution under the influence of UV energy at 0 V bias is defined as the photocurrent per dark current based on the following equation [74, 75]:

$$S = \frac{J_{ph}}{J_{dark}} \tag{12}$$

The values of calculated sensitivity are also presented in Table 4. They illustrate the increase of sensitivity from 232 to 731 with respect to the increase of growth temperature from 115 to 150 °C. This outcome suggests that the sensitivity of grown TNAs mostly depends on the photocurrent value as the dark current value measured at 0 V bias is extremely low.

The rise and fall times of photocurrent under the influence of UV energy of the TNAs/electrolyte heterojunction were also measured. To calculate the response times for each sample, the current density-time switching curves (Fig. 9) measured at 0 V bias were analysed at the rising and falling edges. The rise time is the required time for the photocurrent to increase from 10 to 90% of its maximum value, while the fall time is the required time for the photocurrent to decrease from 90% to 10% of its minimum value. As can be seen from Fig. 8, the rise time is noticeably less than 0.2 s and the fall time is less than 1.0 s as shown in Table 4. Overall, these results indicate that the photocurrent is instantly produced as soon as the UV light is turned on, indicating that the grown TNAs are suitable for high response sensing applications. The photocurrent decay could also be observed at the beginning of the "on" state of UV light in all samples. A strong spike first manifested and gradually diminished until it has been expended to a saturated value of photocurrent. The photocurrent decay may be explained by the fact that the excessive generation of excitonic charge carriers caused by the accumulation of electrons in the bulk or holes on the surface of the grown materials would instantly recombine after being produced [76]. This phenomenon is also possibly due to the inefficient transportation of charge carriers from the TNAs in electrolyte solution under the exposure of UV energy. However, the photocurrent decay in our case could be negligible due to the difference between the maximum spike and the saturated photocurrent values are relatively higher than the dark current value.

In general, the photocurrent is dependent on the photoconductivity effect of the nanorods, which are governed by light-trapping and hole-trapping mechanisms, and the interfacial properties of TNAs/electrolyte, which contains chemisorbed oxygen molecules [77, 78]. These mechanisms are likely to be related to the availability of active surface area. The adsorbed and desorbed oxygen molecules are also corresponded to the rise and fall times upon the interaction with UV energy and became dominant when the materials reached the nanoscale [79]. A high-resistance space charge layer is initially formed at the TNAs/electrolyte interface without any external interference that is likely to be related to the presence of free electrons in n-type TNAs that captured oxygen molecules. The adsorbed oxygen is subsequently desorbed from this space charge layer upon UV illumination to produce excitonic charge carriers, thereby

leading to the generation of photocurrent from the grown TNAs.

In addition, electrochemical impedance spectroscopy (EIS) analysis has been performed to investigate the overall resistance, electron mobility, and recombination of electron–hole pairs at the interface of grown TNAs/electrolyte. The study was performed under UV light (365 nm, 750 μW/cm^2) in a frequency between 0.1 and 10^4 Hz. Figure 11 provides the plot of Nyquist results obtained from the preliminary analysis of EIS for TNAs samples grown at the 115–150 °C temperature range. The equivalent circuit to define the impedance data is shown in the inset of Fig. 11, which corresponds to the charge transfer resistance and capacitance at the TNAs/electrolyte interface (R and C) at an intermediate frequency. The electrolyte/FTO interface at high frequency is represented by the charge transfer resistance (R_{CE}) and Helmholtz capacitance (C_{CE}), while the external circuit at low frequency is represented by the series resistance (R_s) [27, 59, 80]. Overall, the semicircles in the plotted graph represent the R at the intermediate frequency for all samples, which describe the effective surface reaction through the resistance of the grown TNAs under the influence of UV photon energy. R_{CE} and R_s are too small to be seen and considered negligible in the plotted graph, which specifies that the charge transfer at the grown TNAs/electrolyte interface is the dominant factor for contributing the photocurrent under the influence of UV energy. The data for the respective charge transfer resistances were analysed and summarized in Table 5. As can be seen from the table, the R value decreases with increasing length of grown TNAs due to the increase of growth temperature on the 115–150 °C samples. The decline of R could be attributed to the fact that the number of excitonic charge carriers under the influence of UV energy increases with expanding surface areas of grown TNAs.

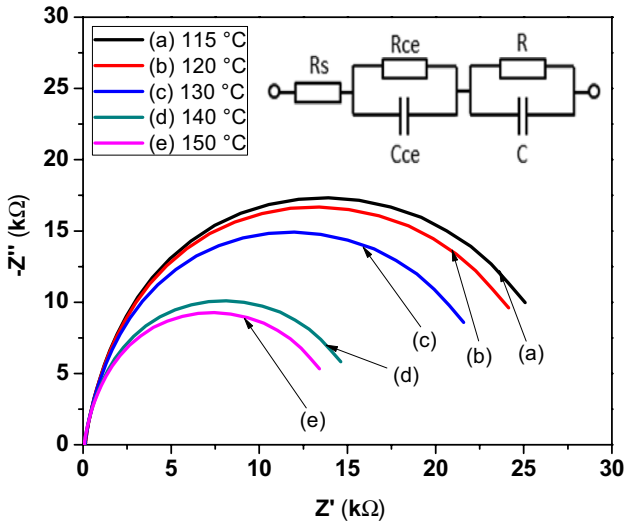

Fig. 11 EIS Nyquist plots of the TNAs-based UV sensor under UV irradiation (365 nm, 750 μW/cm^2)

Table 5 Simulative value of resistances (R_s, R_{CE}, and R) from EIS spectra analysed by equivalent circuit, and lifetime of electrons (τ) of TNAs samples in PEC cell structure

Growth temperature (°C)	R_s (Ω)	R_{CE} (Ω)	R (kΩ)	τ (ms)
115	2.278	0.104	82.597	1.06
120	3.459	0.157	55.170	1.58
130	6.664	0.303	46.031	3.11
140	16.282	0.741	23.943	7.28
150	17.800	0.810	21.850	7.98

Comparison of the findings with those of other studies confirms the association between photocurrent and thickness layer of a grown film [81, 82]. These findings also in line with previous research regarding the correlation between charge transfer resistance and size of grown films [81, 83]. From this result also, we can see that varying the growth temperature resulted in the lowest value of R for the 150 °C sample, replicating that the optimal growth of TNAs yields the maximum number of excitonic charge carriers, and increases the carrier mobility of the grown TNAs. Prior studies have noted the importance of minimising the value of R for enhancing charge transfer through the nanorods with high diffusivity between the grain boundaries and nanoparticles, for lowering electron trapping, and for minimising recombination rate of charge carriers [27, 59, 80, 84]. The results from EIS analysis are also in agreement with the photocurrent values. It can thus be suggested that low charge transfer resistance leads to the increase of charge mobility in the generated photocurrent, and thus increases the responsivity of grown TNAs under the influence of UV energy as shown in Table 5. Moreover, the net loss of excitonic charge carriers during the interaction with UV photons is compensated by the generated photocurrent gain that leads to high photoresponse [83].

Figure 12 displays the Bode-phase plot for grown TNAs on the 115–150 °C samples. The lifetime of electrons (τ) for these samples under the influence of UV photon energy was assessed by the maximum frequency of the peak at the intermediate frequency of the grown TNAs/electrolyte interface from the Bode-phase plot using the following equation [27]:

$$\tau = \frac{1}{2\pi f_{\max}} \tag{13}$$

where $f_{\max}$ is the maximum frequency of the peak. The values of $f_{\max}$ for the grown TNAs samples at 115 °C, 120 °C, 130 °C, 140 °C and 150 °C are 150.53 Hz, 100.54 Hz, 51.06 Hz, 21.81 Hz and 19.91 Hz, respectively. The calculated values of τ are summarized in Table 5. The table illustrates the increase of τ from 1.06 ms to 7.98 ms with

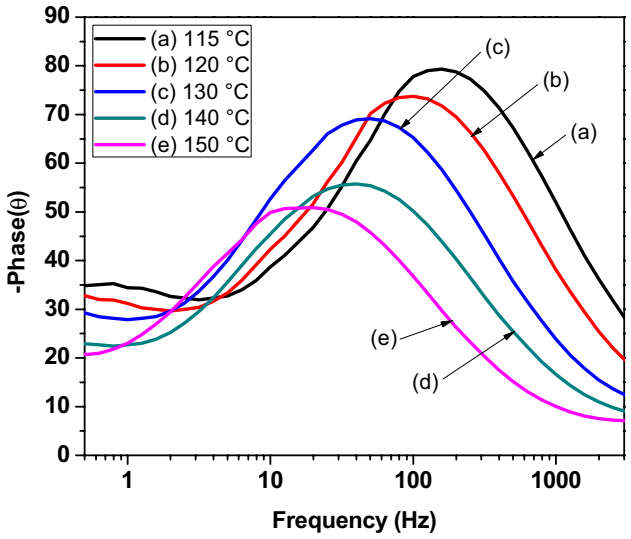

Fig. 12 EIS Bode phase plots under UV irradiation (365 nm, 750 μW/cm^2) of TNAs-based UV sensor

respect to rising growth temperatures of 115–150 °C for the samples. The result indicates that the high surface area of grown TNAs lengthens the path of electron transport towards the conductive substrate, which is associated with more electrolytes permeating into TNAs at higher growth temperatures. This large increase in electron lifetime suppressed the recombination of electrons with the reduced species in the electrolytes. It has also been suggested that the poor contact between TNAs and the FTO substrate could boost the recombination of the carriers at the TNAs/FTO interfaces leading to low photocurrent and electron lifetime [85]. Upon UV illumination, the majority of the excited electrons move toward the FTO substrate, while the photogenerated holes move toward the electrolytes due to the built-in field potential. These photogenerated electrons could be collected by the FTO substrate and then transported to the external circuit to produce the photocurrent. However, the poor contact between the TNAs and FTO could induce recombination of the photogenerated electrons. Furthermore, some of the electrons could be trapped in the lattice defects at the surfaces or interfaces and subsequently recombine with the redox species in the electrolytes. The enlargement of TNAs size with long growth time is expected to improve the contact between TNAs and FTO and thus increase the electron lifetime and photocurrent. Furthermore, the greater crystallite size of TNAs at higher growth temperature as analysed through XRD data facilitate a high surface contact with the FTO substrate and provide smooth carrier transportation across the contacts. The decrease of the R value in accordance to the Nyquist plot (leading to increasing of generated photocurrent) also suggests the efficient interception of charge carrier recombination throughout the grown TNAs/electrolyte interface. Therefore, a longer τ improves the generated photocurrent and responsivity of grown TNAs, which is in agreement to those observed in the Fig. 9. These results imply that TNAs deposited at high growth temperatures bring effective pathways for electron transportation that improve the photocurrent under UV irradiation.

4 Conclusion

The TNAs were successfully grown on the FTO glass substrate without a TiO_2 seed layer by using an improved one-step aqueous chemical growth method in a clamped Schott bottle at different growth temperatures from 115 to 150 °C. FESEM analysis showed that the diameter and length of the grown TNAs increase with increasing growth temperature due to an increase in the nucleation reaction rate. The XRD and Raman analyses revealed that the grown TNAs were crystalline rutile TiO_2. The optical analysis showed that all samples absorbed UV irradiation below 400 nm and the energy bandgap decreased with increasing growth temperature. All grown TNAs samples displayed outstanding responses and highly stable generated photocurrents under the influence of UV energy at 0 V bias in an electrochemical reaction. The generated photocurrent is determined by the effective area of grown TNAs/electrolyte interface for UV absorption. A high generation of photocurrent also decreases the net resistance and occurrence of recombination of charge carriers. In addition, the photocurrent value of grown TNAs under the influence of UV energy could be efficiently tuned by controlling the growth temperature in compliance with detection system requirements. The highest photocurrent value of 150 °C sample was 26.31 μA with a responsivity of 35 mA/W.

Acknowledgements This work was supported by the ASEAN-India Research & Training Fellowship Scheme (IMRC/AISTDF/R&D/P-1/2017). The authors also would like to thank the Institute of Research Management and Innovation (IRMI) of UiTM and the International Islamic University Malaysia (IIUM) for their financial support of this research.

References

1. M. Zhang, D. Li, J. Zhou, W. Chen, S. Ruan, Ultraviolet detector based on TiO_2 nanowire array–polymer hybrids with low dark current. J. Alloy. Compd. **618**, 233–235 (2015)
2. H.Y. Yang, X.-L. Cheng, X.-F. Zhang, Z.-K. Zheng, X.-F. Tang, Y.-M. Xu, S. Gao, H. Zhao, L.-H. Huo, A novel sensor for fast detection of triethylamine based on rutile TiO_2 nanorod arrays. Sens. Actuator B **205**, 322–328 (2014)
3. J. Du, X. Lai, N. Yang, J. Zhai, D. Kisailus, F. Su, D. Wang, L. Jiang, Hierarchically ordered macro–mesoporous TiO_2–graphene composite films: improved mass transfer, reduced charge

recombination, and their enhanced photocatalytic activities. ACS Nano **5**, 590–596 (2011)
4. M. Chen, D.W. Goodman, Catalytically active gold on ordered titania supports. Chem. Soc. Rev. **37**, 1860–1870 (2008)
5. K.-I. Tanaka, H. He, Y. Yuan, Catalytic oxidation of CO on metals involving an ionic process in the presence of H_2O: the role of promoting materials. RSC Adv. **5**, 949–959 (2015)
6. Q. Yue, J. Duan, L. Zhu, K. Zhang, J. Zhang, H. Wang, Effect of HCl etching on TiO_2 nanorod-based perovskite solar cells. J. Mater. Sci. **53**, 15257–15270 (2018)
7. Y. Zhao, X. Gu, R. He, L. Zhu, Y. Qiang, Influence of annealing ambient on the photoelectric and photoelectrochemical properties of TiO_2 nanorod arrays. J. Electron. Mater. **47**, 5251–5258 (2018)
8. H. Choi, H. Ryu, W.-J. Lee, Study of the morphological, optical, structural and photoelectrochemical properties of TiO_2 nanorods grown with various precursor concentrations. Electron. Mater. Lett. **13**, 497–504 (2017)
9. X. Wang, S. Estradé, Y. Lin, F. Yu, L. Lopez-Conesa, H. Zhou, S.K. Gurram, F. Peiró, Z. Fan, H. Shen, L. Schaefer, G. Braeuer, A. Waag, Enhanced photoelectrochemical behavior of H-TiO_2 nanorods hydrogenated by controlled and local rapid thermal annealing. Nanoscale Res. Lett. **12**, 336 (2017)
10. B. Yan, Y. Zhuang, Y. Jiang, W. Xu, Y. Chen, J. Tu, X. Wang, Q. Wu, Enhanced photoeletrochemical biosensing performance from rutile nanorod/anatase nanowire junction array. Appl. Surf. Sci. **458**, 382–388 (2018)
11. L. He, Q. Liu, S. Zhang, X. Zhang, C. Gong, H. Shu, G. Wang, H. Liu, S. Wen, B. Zhang, High sensitivity of TiO_2 nanorod array electrode for photoelectrochemical glucose sensor and its photo fuel cell application. Electrochem. Commun. **94**, 18–22 (2018)
12. X. Yanru, W. Lin, L. Qinghao, C. Yanxue, Y. Shishen, J. Jun, L. Guolei, M. Liangmo, High-performance self-powered UV photodetectors based on TiO_2 nano-branched arrays. Nanotechnology **25**, 075202 (2014)
13. Y. Xie, L. Wei, G. Wei, Q. Li, D. Wang, Y. Chen, S. Yan, G. Liu, L. Mei, J. Jiao, A self-powered UV photodetector based on TiO_2 nanorod arrays. Nanoscale Res. Lett. **8**, 188 (2013)
14. X. Zu, H. Wang, G. Yi, Z. Zhang, X. Jiang, J. Gong, H. Luo, Self-powered UV photodetector based on heterostructured TiO_2 nanowire arrays and polyaniline nanoflower arrays. Synth. Met. **200**, 58–65 (2015)
15. C. Cao, C. Hu, X. Wang, S. Wang, Y. Tian, H. Zhang, UV sensor based on TiO_2 nanorod arrays on FTO thin film, Sens. Actuator B **156**, 114–119 (2011)
16. L. Li, Y. Zhu, X. Lu, M. Wei, W. Zhuang, Z. Yang, X. Feng, Carbon heterogeneous surface modification on a mesoporous TiO_2-supported catalyst and its enhanced hydrodesulfurization performance. Chem. Commun. **48**, 11525–11527 (2012)
17. A.C. Fisher, L.M. Peter, E.A. Ponomarev, A.B. Walker, K.G.U. Wijayantha, Intensity dependence of the back reaction and transport of electrons in dye-sensitized nanocrystalline TiO_2 solar cells. J. Phys. Chem. B **104**, 949–958 (2000)
18. B. van der Zanden, A. Goossens, The nature of electron migration in dye-sensitized nanostructured TiO_2. J. Phys. Chem. B **104**, 7171–7178 (2000)
19. D. Chen, L. Wei, L. Meng, D. Wang, Y. Chen, Y. Tian, S. Yan, L. Mei, J. Jiao, High-performance self-powered UV detector based on SnO_2-TiO_2 nanomace arrays. Nanoscale Res. Lett. **13**, 92 (2018)
20. D. Chen, L. Wei, L. Meng, D. Wang, Y. Chen, Y. Tian, S. Yan, L. Mei, J. Jiao, Visible-blind quasi-solid-state UV detector based on SnO_2-TiO_2 nanoheterostructure arrays. J. Alloy. Compd. **751**, 56–61 (2018)
21. Y. Wang, M. Zu, S. Li, T. Butburee, L. Wang, F. Peng, S. Zhang, Dual modification of TiO_2 nanorods for selective photoelectrochemical detection of organic compounds. Sens. Actuator B **250**, 307–314 (2017)
22. P. Yan, Y. Wu, G. Liu, A. Li, H. Han, Z. Feng, J. Shi, Y. Gan, C. Li, Enhancing photoresponsivity of self-powered UV photodetectors based on electrochemically reduced TiO_2 nanorods. RSC Adv. **5**, 95939–95942 (2015)
23. K. Zhu, N.R. Neale, A. Miedaner, A.J. Frank, Enhanced charge-collection efficiencies and light scattering in dye-sensitized solar cells using oriented TiO_2 nanotubes arrays. Nano Lett. **7**, 69–74 (2007)
24. M. Rajabi, S. Shogh, A. Iraji zad, Defect study of TiO_2 nanorods grown by a hydrothermal method through photoluminescence spectroscopy. J. Lumin. **157**, 235–242 (2015)
25. X. Feng, K. Shankar, O.K. Varghese, M. Paulose, T.J. Latempa, C.A. Grimes, Vertically aligned single crystal TiO_2 nanowire arrays grown directly on transparent conducting oxide coated glass: synthesis details and applications. Nano Lett. **8**, 3781–3786 (2008)
26. J. Wu, S. Lo, K. Song, B.K. Vijayan, W. Li, K.A. Gray, V.P. Dravid, Growth of rutile TiO_2 nanorods on anatase TiO_2 thin films on Si-based substrates. J. Mater. Res. **26**, 1646–1652 (2011)
27. Y. Xie, L. Wei, Q. Li, Y. Chen, H. Liu, S. Yan, J. Jiao, G. Liu, L. Mei, A high performance quasi-solid-state self-powered UV photodetector based on TiO_2 nanorod arrays. Nanoscale **6**, 9116–9121 (2014)
28. P. Zhao, S. Yao, M. Wang, B. Wang, P. Sun, F. Liu, X. Liang, Y. Sun, G. Lu, High-efficiency dye-sensitized solar cells with hierarchical structures titanium dioxide to transfer photogenerated charge. Electrochim. Acta **170**, 276–283 (2015)
29. H. Cheng, J. Ma, Z. Zhao, L. Qi, Hydrothermal preparation of uniform nanosize rutile and anatase particles. Chem. Mater. **7**, 663–671 (1995)
30. B. Liu, E.S. Aydil, Growth of oriented single-crystalline rutile TiO_2 nanorods on transparent conducting substrates for dye-sensitized solar cells. J. Am. Chem. Soc. **131**, 3985–3990 (2009)
31. S.S. Pradhan, S.K. Pradhan, V. Bhavanasi, S. Sahoo, S.N. Sarangi, S. Anwar, P.K. Barhai, Low temperature stabilized rutile phase TiO_2 films grown by sputtering. Thin Solid Films **520**, 1809–1813 (2012)
32. V. Jordan, U. Javornik, J. Plavec, A. Podgornik, A. Rečnik, Self-assembly of multilevel branched rutile-type TiO_2 structures via oriented lateral and twin attachment. Sci. Rep. **6**, 24216 (2016)
33. J.E. House, K.A. House, *Descriptive Inorganic Chemistry*, 2nd edn. (Elsevier Inc, Oxford, 2010)
34. M. Gopal, W.J. Moberly Chan, L.C. De Jonghe, Room temperature synthesis of crystalline metal oxides. J. Mater. Sci. **32**, 6001–6008 (1997)
35. B.S. Buyuktas, Investigation of the complexation and hydrolysis–condensation of titanium(IV) n-butoxide [Ti(OBun)4] with some unsaturated mono and dicarboxylic acids. Trans. Met. Chem. **31**, 786–791 (2006)
36. J. Livage, M. Henry, C. Sanchez, Sol-gel chemistry of transition metal oxides. Prog. Solid State Chem. **18**, 259–341 (1988)
37. J.-P. Jolivet, M. Henry, J. Livage, *Metal Oxide Chemistry and Synthesis* (Wiley, Chichester, 2000)
38. M. Henry, J.-P. Jolivet, J. Livage, *Aqueous Chemistry of Metal Cations: Hydrolysis, Condensation and Complexation* (Springer, Berlin, 1992)
39. J. Su, L. Guo, High aspect ratio TiO_2 nanowires tailored in concentrated HCl hydrothermal condition for photoelectrochemical water splitting. RSC Adv. **5**, 53012–53018 (2015)
40. V. Etacheri, M.K. Seery, S.J. Hinder, S.C. Pillai, Oxygen rich titania: a dopant free, high temperature stable, and visible-light active anatase photocatalyst. Adv. Funct. Mater. **21**, 3744–3752 (2011)

41. Y. Shao, D. Tang, J. Sun, Y. Lee, W. Xiong, Lattice deformation and phase transformation from nano-scale anatase to nano-scale rutile TiO_2 prepared by a sol-gel technique. China Part. **2**, 119–123 (2004)
42. M.F. Malek, M.H. Mamat, Z. Khusaimi, M.Z. Sahdan, M.Z. Musa, A.R. Zainun, A.B. Suriani, N.D. Md, S.B. Sin, M. Abd Hamid, Rusop, Sonicated sol–gel preparation of nanoparticulate ZnO thin films with various deposition speeds: the highly preferred c-axis (0 0 2) orientation enhances the final properties. J. Alloy. Compd. **582**, 12–21 (2014)
43. L. Miao, S. Tanemura, Y. Kondo, M. Iwata, S. Toh, K. Kaneko, Microstructure and bactericidal ability of photocatalytic TiO_2 thin films prepared by rf helicon magnetron sputtering. Appl. Surf. Sci. **238**, 125–131 (2004)
44. A.M. Selman, Z. Hassan, Growth and characterization of rutile TiO_2 nanorods on various substrates with fabricated fast-response metal–semiconductor–metal UV detector based on Si substrate. Superlattices Microstruct. **83**, 549–564 (2015)
45. L. Meng, H. Chen, C. Li, M.P. dos Santos, Growth of the [110] oriented TiO_2 nanorods on ITO substrates by sputtering technique for dye-sensitized solar cells. Front. Mater. **1**, 14 (2014)
46. C.V. Thompson, Structure evolution during processing of polycrystalline films. Annu. Rev. Mater. Sci. **30**, 159–190 (2000)
47. M. Ye, D. Zheng, M. Lv, C. Chen, C. Lin, Z. Lin, Hierarchically structured nanotubes for highly efficient dye-sensitized solar cells. Adv. Mater. **25**, 3039–3044 (2013)
48. F. Shao, J. Sun, L. Gao, S. Yang, J. Luo, Forest-like TiO_2 hierarchical structures for efficient dye-sensitized solar cells. J. Mater. Chem. **22**, 6824–6830 (2012)
49. M.J. Alam, D.C. Cameron, Preparation and properties of transparent conductive aluminum-doped zinc oxide thin films by sol–gel process. J. Vac. Sci. Technol. A **19**, 1642–1646 (2001)
50. M. Zhang, M. Zhang, S. Shi, X. Song, Z. Sun, An approach toward TiO_2 nanostructure growth with tunable properties: influence of reaction time in a hydrothermal process. J. Alloy. Compd. **591**, 213–217 (2014)
51. P. Jain, P. Arun, Influence of grain size on the band-gap of annealed SnS thin films. Thin Solid Films **548**, 241–246 (2013)
52. C.R. Aita, Raman scattering by thin film nanomosaic rutile TiO_2. Appl. Phys. Lett. **90**, 213112 (2007)
53. X. Shen, J. Zhang, B. Tian, Microemulsion-mediated solvothermal synthesis and photocatalytic properties of crystalline titania with controllable phases of anatase and rutile. J. Hazard. Mater. **192**, 651–657 (2011)
54. Q. Gao, X. Wu, Y. Fan, X. Zhou, Low temperature synthesis and characterization of rutile TiO_2-coated mica–titania pigments. Dyes Pigm. **95**, 534–539 (2012)
55. S.-M. Oh, T. Ishigaki, Preparation of pure rutile and anatase TiO_2 nanopowders using RF thermal plasma. Thin Solid Films **457**, 186–191 (2004)
56. V. Swamy, Size-dependent modifications of the first-order Raman spectra of nanostructured rutile TiO_2. Phys. Rev. B **77**, 195414 (2008)
57. D. Wang, J. Zhao, B. Chen, C. Zhu, Lattice vibration fundamentals in nanocrystalline anatase investigated with Raman scattering. J. Phys. Condes. Matter **20**, 085212 (2008)
58. W.F. Zhang, Y.L. He, M.S. Zhang, Z. Yin, Q. Chen, Raman scattering study on anatase TiO_2 nanocrystals. J. Phys. D **33**, 912 (2000)
59. S.S. Mali, C.S. Shim, H. Kim, C.K. Hong, Single step synthesized 1D TiO_2 vertically aligned nanorod arrays for CdS sensitized quantum dot sensitized solar cells. Ceram. Int. **42**, 1973–1981 (2016)
60. N.J. Kim, Y.H. La, S.H. Im, B.K. Ryu, Optical and structural properties of Fe–TiO_2 thin films prepared by sol–gel dip coating. Thin Solid Films **518**, 156–160 (2010)
61. S. Sadhu, P. Poddar, Template-free fabrication of highly-oriented single-crystalline 1D-rutile TiO_2-MWCNT composite for enhanced photoelectrochemical activity. J. Phys. Chem. C **118**, 19363–19373 (2014)
62. S. Batakrushna, P.K. Giri, I. Kenji, F. Minoru, Microscopic origin of lattice contraction and expansion in undoped rutile TiO_2 nanostructures. J. Phys. D **47**, 215302 (2014)
63. S. Savaş, A. Aysun, S. Tülay, S. Necmi, The effects of film thickness on the optical properties of TiO_2–SnO_2 compound thin films. Phys. Scr. **84**, 065602 (2011)
64. M. Landmann, E. Rauls, W.G. Schmidt, The electronic structure and optical response of rutile, anatase and brookite TiO_2. J. Phys. Condes. Matter **24**, 195503 (2012)
65. J. Zhang, P. Zhou, J. Liu, J. Yu, New understanding of the difference of photocatalytic activity among anatase, rutile and brookite TiO_2. Phys. Chem. Chem. Phys. **16**, 20382–20386 (2014)
66. Y.P. He, Z.Y. Zhang, Y.P. Zhao, Optical and photocatalytic properties of oblique angle deposited TiO_2 nanorod array. J. Vac. Sci. Technol. B **26**, 1350–1358 (2008)
67. N.K. Allam, M.A. El-Sayed, Photoelectrochemical water oxidation characteristics of anodically fabricated TiO_2 nanotube arrays: structural and optical properties. J. Phys. Chem. C **114**, 12024–12029 (2010)
68. N.R. Mathews, E.R. Morales, M.A. Cortés-Jacome, J.A. Toledo Antonio, TiO_2 thin films–influence of annealing temperature on structural, optical and photocatalytic properties. Sol. Energy **83**, 1499–1508 (2009)
69. R. Wang, K. Hashimoto, A. Fujishima, M. Chikuni, E. Kojima, A. Kitamura, M. Shimohigoshi, T. Watanabe, Photogeneration of highly amphiphilic TiO_2 surfaces. Adv. Mater. **10**, 135–138 (1998)
70. M. Miyauchi, N. Kieda, S. Hishita, T. Mitsuhashi, A. Nakajima, T. Watanabe, K. Hashimoto, Reversible wettability control of TiO_2 surface by light irradiation. Surf. Sci. **511**, 401–407 (2002)
71. K. Hatta, M. Higuchi, J. Takahashi, K. Kodaira, Floating zone growth and characterization of aluminum-doped rutile single crystals. J. Cryst. Growth **163**, 279–284 (1996)
72. M. Razeghi, A. Rogalski, Semiconductor ultraviolet detectors. J. Appl. Phys. **79**, 7433 (1996)
73. A. Ghasempour Ardakani, M. Pazoki, S.M. Mahdavi, A.R. Bahrampour, N. Taghavinia, Ultraviolet photodetectors based on ZnO sheets: the effect of sheet size on photoresponse properties. Appl. Surf. Sci. **258**, 5405–5411 (2012)
74. Z. Alaie, S. Mohammad Nejad, M.H. Yousefi, Recent advances in ultraviolet photodetectors. Mater. Sci. Semicond. Process. **29**, 16–55 (2015)
75. B. Yuan, X.J. Zheng, Y.Q. Chen, B. Yang, T. Zhang, High photosensitivity and low dark current of photoconductive semiconductor switch based on ZnO single nanobelt. Solid-State Electron. **55**, 49–53 (2011)
76. L. Zhang, E. Reisner, J.J. Baumberg, Al-doped ZnO inverse opal networks as efficient electron collectors in $BiVO_4$ photoanodes for solar water oxidation. Energy Environ. Sci. **7**, 1402–1408 (2014)
77. T. Zhai, L. Li, X. Wang, X. Fang, Y. Bando, D. Golberg, Recent developments in one-dimensional inorganic nanostructures for photodetectors. Adv. Funct. Mater. **20**, 4233–4248 (2010)
78. J.D. Prades, F. Hernandez-Ramirez, R. Jimenez-Diaz, M. Manzanares, T. Andreu, A. Cirera, A. Romano-Rodriguez, J.R. Morante, The effects of electron–hole separation on the photoconductivity of individual metal oxide nanowires. Nanotechnology **19**, 465501 (2008)
79. X. Li, C. Gao, H. Duan, B. Lu, X. Pan, E. Xie, Nanocrystalline TiO_2 film based photoelectrochemical cell as self-powered UV-photodetector. Nano Energy **1**, 640–645 (2012)
80. P.B. Patil, S.S. Mali, V.V. Kondalkar, K.V. Khot, R.M. Mane, C.K. Hong, P.S. Patil, J.H. Kim, P.N. Bhosale, An approach towards TiO_2 chrysanthemum flowers with tunable properties: influence

of reaction time in hydrothermal process. J. Mater. Sci. **26**, 6119–6128 (2015)
81. A. Mathew, G.M. Rao, N. Munichandraiah, Effect of TiO_2 electrode thickness on photovoltaic properties of dye sensitized solar cell based on randomly oriented Titania nanotubes. Mater. Chem. Phys. **127**, 95–101 (2011)
82. C.-P. Hsu, K.-M. Lee, J.T.-W. Huang, C.-Y. Lin, C.-H. Lee, L.-P. Wang, S.-Y. Tsai, K.-C. Ho, EIS analysis on low temperature fabrication of TiO_2 porous films for dye-sensitized solar cells. Electrochim. Acta **53**, 7514–7522 (2008)
83. H. Li, Q. Yu, Y. Huang, C. Yu, R. Li, J. Wang, F. Guo, S. Jiao, S. Gao, Y. Zhang, X. Zhang, P. Wang, L. Zhao, Ultralong rutile TiO_2 nanowire arrays for highly efficient dye-sensitized solar cells. ACS Appl. Mater. Interfaces **8**, 13384–13391 (2016)
84. M. Zhu, L. Chen, H. Gong, M. Zi, B. Cao, A novel TiO_2 nanorod/nanoparticle composite architecture to improve the performance of dye-sensitized solar cells. Ceram. Int. **40**, 2337–2342 (2014)
85. Y. Zhao, X. Gu, Y. Qiang, Influence of growth time and annealing on rutile TiO_2 single-crystal nanorod arrays synthesized by hydrothermal method in dye-sensitized solar cells. Thin Solid Films **520**, 2814–2818 (2012)